LAWRENCE
LIVERMORE
NATIONAL
LABORATORY

LLNL-JRNL-521551

# Relation Between Electric and Magnetic Field Structures and Their Proton Beam Images

N. L. Kugland, D. D. Ryutov, C. Plechaty, J. S. Ross, H. -S. Park

December 23, 2011

Review of Scientific Instruments

## Disclaimer

# Relation between electric and magnetic field structures and their proton-beam images

**N.L. Kugland, D.D. Ryutov, C. Plechaty, J.S. Ross, H.-S. Park**

Lawrence Livermore National Laboratory, Livermore, CA 94551

## Abstract

Proton imaging is commonly used to detect electric and magnetic fields in laser-produced plasmas with high spatial and temporal resolution. However, the analysis methods for this diagnostic can be cumbersome, the typical approach being to numerically ray trace a very large number of protons through assumed fields. Presented here is a set of compact analytic equations for proton imaging that relate the observed distribution of protons in the image plane to the electric and magnetic fields in the object. Inversion of the images is considered. Smooth electric and magnetic field structures are seen to produce sharp features in the image plane (analogous to optical caustics) if the fields are sufficiently strong. Characteristic features of the intensity distribution near the caustics are discussed. Limitations on the spatial and temporal resolution are assessed. A set of analytical models suitable for helping in the interpretation of experimentally obtained images and for code benchmarking is described. Results presented can serve as a starting point for accelerated analysis of proton imaging results, providing an efficient approach that can be extended to additional characteristic shapes in the future.

## I. INTRODUCTION

Point-projection proton imaging (also known as proton radiography or proton deflectometry) is established as a highly useful technique for the diagnosis of high-energy-density laboratory plasmas [Li 2010, Cecchetti 2009, Li 2009, Romagnani 2008]. A weakly divergent, polyenergetic proton beam suitable for radiography can be produced by irradiating a thin metal foil by a short laser pulse [Borghesi 2004, Mackinnon 2004, Roth 2011, Borghesi 2008]. Alternatively, one can use the laser-driven implosion of a D-$^3$He capsule, which produces an essentially spherically-symmetric, short pulse of protons at stagnation [Li 2010, Li 2009]. The proton energy is typically 5 – 50 MeV in the first approach and 14.7 MeV in the second approach. Sending the protons through the object of interest makes images of electromagnetic and density structures with exquisite spatial resolution (few-micron scale) and very good temporal resolution (10 ps scale).

For mm-scale plasmas with densities in the range of $10^{17}$-$10^{21}$ cm$^{-3}$ (areal densities in the range of $10^{16}$-$10^{20}$ cm$^{-2}$), where collisional scattering of the proton beam can be neglected, proton radiography may be the only diagnostic technique available today that is capable of high-performance imaging of electromagnetic fields over a wide range of field strengths [Roth 2011]. This application will be the main subject of our paper.

Our study was motivated by experiments on collisionless shocks [Ross 2012, Park 2012, Loupias 2009, Gregory 2010, Kuramitsu 2011, Constantin 2009], where significant electric and magnetic fields are expected to be generated in the zone of the intersection of two high-velocity plasma jets. Our numerical examples will be mostly related to this type of the experiment. On the other hand, the general derivations and resulting equations are of a broader use and can be applied to other systems as well. We aim at producing simple analytical relations to assist in the interpretation of experimental results, as guidance for more detailed numerical analyses and for rough evaluation of the applicability/inapplicability of proton radiography in any specific setting.

A schematic of a typical proton imaging experiment is shown in Fig. 1. The proton source is located a distance $l$ from a three-dimensional electric or magnetic field structure of a characteristic size (in both the transverse and longitudinal directions) $2a<<l$. We introduce a coordinate frame $(x, y, z)$ with the origin situated somewhere within the object, and axis $z$ passing through the proton source. We call the plane $z=0$ "an object plane" for the following reason: although the perturbations forming the object are three-dimensional, they are nevertheless localized near this plane. What is important in further derivations is the assumption that the distance $l$ is large compared to the object size (a paraxial model). We will consider a variety of characteristic plasma structures, such as the Gaussian "blob" of electrostatic potential shown in Fig. 2, and calculate the proton images that they produce, some of which are shown in Fig. 3. In a real plasma, one is likely to encounter several structures close to each other, a case that is illustrated in Fig. 4. It should be noted that the deflection from multiple structures is in general non-linear, i.e. not merely a superposition of the individual deflections. This can result in strangely shaped image features with morphologies that bear little resemblance to the parent structure in the object plane.

We start under the assumption that the proton source is a point source and later discuss effects related to its finite size. We assume that the electromagnetic fields of the disturbance can be regarded as static during the proton transit time (less than about 20 ps for $2a < 1$ mm and $\approx 10$ MeV protons). The detector, typically one or more sheets of radiochromic film [Roth 2011, Hey 2008], is located in the image plane at a distance $L>>l$ from the object plane. Higher order corrections to these approximations are considered in Sec. VI.

Our paper is organized as follows. First, we show the general mapping of protons from the object plane to the image plane, which can be used to calculate synthetic proton images from arbitrary disturbances. Second, we present an efficient inversion technique for the case of a modest intensity variation, Third, we introduce the concept of optical caustic formation, and develop the mathematics for identifying such caustics from both electric and magnetic perturbations. Finally, we present examples of the images from some specific types of perturbations, like ellipsoidal-shape perturbations, strongly elongated 2D perturbations, and perturbations with sharp fronts (like the ones that are anticipated in the presence of shocks). Some more lengthy calculations are presented in the Appendices.

## II. THE BASIC MAPPING

Let us start by considering the basic optics of point projection imaging. We use the intersection point of a particular proton beamlet ("ray") with the object plane, $x_0$, $y_0$, as a tag for this beamlet. There are two, generally independent, small parameters in our problem.

The first is the paraxiality parameter, $a/l$. It is typically in the range of 0.1. One can restate the presence of this small parameter in terms of the ratios $x_0/l$ and $y_0/l$ which both need to be much less than 1. The position of the same beamlet in the image plane is denoted by $x,y$ (no subscript).

The second small parameter is the deflection angle $\alpha$ of the beamlet passing through the electromagnetic perturbations; deflections in the $x$ and $y$ directions are characterized by the angles $\alpha_x(x_0,y_0)$ and $\alpha_y(x_0,y_0)$, respectively. As we see in the numerical examples of the further sections, these angles are also small, typically less than or comparable to $a/l$.

In evaluating deflection, we retain only terms up to the leading essential order in the parameters $a/l$ and $\alpha$. The higher-order terms would create small corrections (see Sec.VI). In the leading essential order, the point $x_0$, $y_0$ in the object plane will be mapped to the points

$$x = x_0 + \frac{x_0}{l}L + \alpha_x L, \tag{1}$$

$$y = y_0 + \frac{y_0}{l}L + \alpha_y L, \tag{2}$$

in the image plane. Note that we approximate $\sin\alpha = \tan\alpha = \alpha$. The lateral displacement of the beam during the interaction with the object is neglected here, as it is of the order of $\alpha a << \alpha L$. In other words, the main contribution to the image formation comes from the angular deflection, not from a small lateral displacement of the proton in the interaction zone. To find a synthetic image, one must therefore find $\alpha_x(x_0,y_0)$ and $\alpha_y(x_0,y_0)$.

To have a significant magnification of the object, one places the image plane much further from the object than the distance between the object and the proton source, $L>>l$. Typically, $L$ is 10-30 times greater than $l$. In such a case, one can neglect the first term in the right-hand-side of Eqs. (1), (2) compared to the second term, thereby arriving at the simplified equations

$$x = L\left(\frac{x_0}{l} + \alpha_x\right), \tag{1'}$$

$$y = L\left(\frac{y_0}{l} + \alpha_y\right). \tag{2'}$$

In this limit, the distance $L$ scales out of the final *shape* of the image and is responsible only for the *size* of the image.

The presence of the functions $\alpha_x(x_0,y_0)$ and $\alpha_y(x_0,y_0)$ in the mapping (1), (2) means that in the image plane the object is not only magnified but also distorted, as illustrated in Fig. 4. In this respect, the situation is different from contrast radiography with no deflection ($\alpha = 0$), where the object is just magnified, with magnification being $M = 1 + L/l$ . The sensitivity of imaging to deflection angle in our case is important: to

generate qualitatively correct non-linear images of the type that are characteristic of strong proton deflection, as well as to make accurate quantitative statements about the size and shape of the electromagnetic disturbances observed by proton imaging, one must take care to include the deflection term $\alpha \neq 0$ when making calculations. We will return to this topic later in the paper.

The surface element $dS_0$ in the object plane is mapped to the surface element $dS$ in the image plane, and the two are related via the Jacobian determinant:

$$dS = \left| \frac{\partial(x,y)}{\partial(x_0,y_0)} \right| dS_0 \,. \tag{3}$$

The "rays" (protons) passing through the surface element $dS_0$ then pass also through the surface element $dS$ meaning that the intensity in the image plane is proportional to the intensity in the object plane, multiplied by $(dS_0/dS)$. The intensity distribution in the image plane can therefore be represented using the reciprocal of the Jacobian determinant:

$$I = \frac{I^*}{\left| \frac{\partial(x,y)}{\partial(x_0,y_0)} \right| + \varepsilon}, \tag{4}$$

where $I^*$ is the intensity distribution in the object plane (essentially uniform) and $\varepsilon > 0$ is a small parameter that limits the intensity in the image plane; its origin can be related to the finite brightness of the probe beam and/or finite resolution of the radiochromic film. Equation 4 can be used to generate synthetic proton imagery once one has identified the functional form of the deflection angles $\alpha(x_0, y_0)$. Later in this paper, we will derive these deflection angles for protons moving through electric and magnetic potentials of the type that might be found in laser-produced plasmas.

For the transformations (1) and (2), the Jacobian acquires the form

$$\left| \frac{\partial(x,y)}{\partial(x_0,y_0)} \right| = \left| \left(1 + \frac{L}{l} + \frac{\partial \alpha_x}{\partial x_0} L\right)\left(1 + \frac{L}{l} + \frac{\partial \alpha_y}{\partial y_0} L\right) - L^2 \frac{\partial \alpha_x}{\partial y_0}\frac{\partial \alpha_y}{\partial x_0} \right| \tag{5}$$

In the most interesting case of a strong magnification, when simplified equations (1'), (2') are valid, one can use the following relation

$$\left| \frac{\partial(x,y)}{\partial(x_0,y_0)} \right| = L^2 \left| 1 + l\left( \frac{\partial \alpha_x}{\partial x_0} + \frac{\partial \alpha_y}{\partial y_0} \right) + l^2 \left( \frac{\partial \alpha_x}{\partial x_0}\frac{\partial \alpha_y}{\partial y_0} - \frac{\partial \alpha_x}{\partial y_0}\frac{\partial \alpha_y}{\partial x_0} \right) \right| \tag{5'}$$

Thus far we considered the images created by a point source and large magnification, i.e. $l << L$. The projection by a parallel set of rays can also be of some interest (if not for experiments, then for theory models and simulations). It would formally correspond to an opposite limiting case $l >> L$. In this case, one can still use Eqs. (1), (2), but would have to drop the second term in the r.h.s. of these equations. Therefore, the shape of the image for the projection by a parallel beam depends on the distance $L$ between the object and the film. For large-enough $L$, such that $\alpha L >> a$, the mapping again becomes scale-invariant with respect to $L$. The shape of the images, however, becomes quite different from that determined by the point projection, $l << L$.

## III. WEAK AND STRONG INTENSITY VARIATIONS

When analyzing Eq. (4), one has to distinguish between two qualitatively different cases: the first, where deflection angles are so small that the Jacobian only slightly differs from unity, and the second, where deflection angles are larger, so that the Jacobian may turn zero at some points, meaning a significant increase of intensity at these points in the image plane. The points of high intensity usually form lines in the image plane (see below). These lines are intersections of the image plane with so called caustic surfaces [Nye 1999]. We consider these two cases consecutively in this section.

Before doing that, we identify a dimensionless parameter whose magnitude determines which case we are dealing with. If the deflection is created by an electromagnetic perturbation of a spatial scale $a$, and the characteristic deflection angle is $\alpha$, the spatial derivatives of $\alpha$ that enter Eq. (5') can be estimated as $\alpha/a$. Then, the term proportional to $l$ in Eq. (5') can be estimated as $\ell\alpha/a$. We denote this dimensionless parameter as $\mu$:

$$\mu = \ell\alpha / a . \tag{6}$$

If this dimensionless parameter is much smaller than 1, the relative spatial variation of the Jacobian (5') is also small. Conversely, if this parameter becomes of order 1, the variation becomes significant, and non-linear features such as caustics or strange shapes can appear.

In the case where $\mu$ is small, one can neglect the second-order terms in Eq. (5'); likewise, one can neglect the small parameter $\varepsilon$ in the denominator of Eq. (4). This gives rise to the following expression for the intensity distribution in the image plane:

$$I = I_0\left[1 - l\left(\frac{\partial\alpha_x}{\partial x_0} + \frac{\partial\alpha_y}{\partial y_0}\right)\right] \tag{7}$$

The coefficient $I_0$ is the intensity in the image plane in the absence of any perturbations. We consider it as being uniform over the size of the image.

Note that a weakly varying intensity in the image plane does not mean that the electromagnetic fields in a plasma are weak with respect to plasma dynamics: they can in particular correspond to strongly nonlinear plasma waves. Nevertheless, the observed intensity perturbations can still be weak because of a high probe beam proton energy $W$.

The intensity in Eq. (7) is expressed in terms of the coordinates $x_0$, $y_0$ in the object plane, whereas the observation is made in the image plane. To express the intensity in terms of $x,y$, one has to use the mapping (1'), (2'). Here, in the limit of $\mu<<1$, one can neglect the terms proportional to $\alpha$, and use the mapping

$$x = \frac{L}{l}x_0; \quad y = \frac{L}{l}y_0, \tag{8}$$

In this case, the magnification is uniform over the object and equal to $M=1+L/l$.

If the parameter $\mu$ approaches or exceeds unity, one has to use the full set of equations (1'), (2'), (4) and (5'). For the known functions $\alpha_x(x_0,y_0)$and $\alpha_y(x_0,y_0)$ this set of equations yields an intensity distribution $I(x,y)$ in the object plane via the parametric dependence $x=x(x_0, y_0)$, $y=y(x_0, y_0)$, provided by the mapping (1'), (2').

The condition

$$D(x_0, y_0) \equiv \left| \frac{\partial(x, y)}{\partial(x_0, y_0)} \right| = 0 \qquad (9)$$

defines one-dimensional manifolds (lines) on which the intensity reaches high values, limited, as mentioned above, by the finite brightness of the source and finite resolution of the detector. In some exceptional cases the lines may degenerate into points.

Mathematically, caustics correspond to the situation where *dS* in Eq. 3 is zero, signifying a high (formally, infinite) intensity in the image plane. In our model, the finite resolution parameter $\varepsilon$ prevents the intensity from actually becoming infinite; this parameter can be neglected at some (small) distance from the caustic.

These singular lines are a manifestation of a more general phenomenon, the formation of the caustic surfaces that are well known in optics (e.g. [Nye 1999]). The intersection of the image plane with a caustic surface is the aforementioned singular line. For brevity, we call these lines themselves "the caustics." The caustics, if formed, make a "skeleton" of the overall image and carry important information about the perturbation, as discussed below. Note that the condition $\mu \sim 1$ can still be compatible with a small-angle deflection approximation if $a << l$, as we assume. In our analysis we see non-linear features appearing for $1 < \mu < 2$.

Finding a caustic in our case consists of the following two steps. First, we solve Eq. (9) and find an implicit equation $D(x_0, y_0) = 0$ for the projection of the caustic onto the object plane. Note that since there is no real caustic in the object plane, the intensity there is essentially uniform. The projection of the line $D(x_0, y_0) = 0$ to the object plane along the rays (1'), (2') yields an actual caustic. This is the second step in finding the caustic in the object plane: moving along the curve $D(x_0, y_0) = 0$ and projecting each point on this curve to the image plane. In a general case, this is a rather cumbersome exercise. Some examples are given in Sec. VI.

If a caustic is formed, the intensity variation in the direction *normal* to the caustic in the image plane has a universal shape. Indeed, in the vicinity of the line $D(x,y)=0$ the function $D$ varies linearly with the distance $\xi$ in the direction normal to the caustic, so that on the caustic itself ($\xi = 0$) the function $D$ becomes zero. One can note that the requirement that the normal derivative is zero, so that the expansion of $D$ starts from the term $\sim \xi^2$, would define a point and is therefore of less interest. So, the intensity variation across the caustic has a universal form,

$$\frac{I}{I_0} \approx \frac{1}{C\,|\xi| + \varepsilon}, \qquad (10)$$

with $C$ being a constant (which may vary along the caustic). For a good-enough resolution, the parameter $\varepsilon$ is small, and there exists a range of $\xi$ in which the intensity varies as $1/|\xi|$. At larger distances, this distribution merges with smooth, $\sim 1$, variations of intensity. In order for the presentation (10) to have some range of applicability, the intensity contrast between the caustic and surrounding areas must be large, by a factor of a few.

This paper deals with the objects that contain a few arbitrarily located, possibly overlapping, field structures, so that every beamlet "sees" not too many of them on its way through the object. If the structures become very small in size, and are randomly distributed in space, their cumulative effect on the beamlet becomes different from that

described in this paper, and the interaction of the beamlet with these random fields then has to be described in terms of a small-angle scattering. The emerging beamlet is then not only deflected, but also broadened. The broadening may smear out fine features of the type that are characteristic of caustics. The broadening itself, on the other hand, would carry information about small-scale random fields. We leave the analysis of the superposition of these two effects for future work.

## IV. DEFLECTION BY AN ELECTROSTATIC FIELD

### A. General expression

Small deflection angles can be found by the perturbative technique. The deflection angle $\alpha_{x,y}$ is given by the (small) acquired transverse velocity $v_{x,y}$, divided by the approximately constant forward velocity $v = v_z$. To illustrate, the x-component of the deflection can be found from

$$\frac{dv_x}{dt} = -\frac{e}{m}\frac{\partial \phi}{\partial x}, \tag{11}$$

where $e$ and $m$ are the proton charge and mass, respectively, and $\phi$ is the electrostatic potential. The right-hand side is taken at the instantaneous position of the particle on the unperturbed trajectory. To obtain $v_x$, we make use of the fact that $dz = v_z\, dt$ to remove the time dependence and find that

$$v_x = -\frac{e}{m v_z}\int_{-\infty}^{+\infty} \frac{\partial \phi(x_0, y_0, z_0)}{\partial x_0} dz_0 . \tag{12}$$

We write here a subscript "0" to emphasize that the action occurs in the object location. One then has:

$$\alpha_x = -\frac{e}{2W}\frac{\partial}{\partial x_0}\int_{-\infty}^{+\infty} \varphi(x_0, y_0, z_0) dz_0 ; \quad \alpha_y = -\frac{e}{2W}\frac{\partial}{\partial y_0}\int_{-\infty}^{+\infty} \varphi(x_0, y_0, z_0) dz_0 , \tag{13}$$

where $W = \frac{1}{2}\, m v_z^2$ is the proton beam energy. When making these calculations, we neglect terms of higher order in the parameters $a/l$ and $\alpha$. In particular, the trajectory along which integration is performed is approximated by a line parallel to the $z$ axis, a good assumption in the (small) region where $\varphi \neq 0$. Retaining the higher-order terms would have led to the appearance of small corrections to Eq. (13), of a magnitude $\sim \alpha a/l$, $\alpha^2$, etc (See Sec. VI for more details).

The lateral spatial displacement acquired during the passage of the proton through the object can be found by integrating $v_{x,y}$ over time. This displacement is $\sim \alpha a$. Adding it to the r.h.s. of Eqs. (1'), (2') leads to an insignificant correction to the mapping: this correction is much smaller than even already neglected terms $x_0, y_0 \sim a$. The condition for neglecting the proton displacement may be more restrictive in the case where the potential distribution has two significantly different spatial scales. This can be, for example, the case of a shock structure with an overall size $a$, but with the thickness $h << a$. We discuss this situation in Sec. IV C.

### B. Inversion problem for small intensity variation

In the case of a small intensity variation, one can invert an intensity map and obtain a spatial (2-dimensional) distribution of a quantity

$$\Phi(x_0, y_0) \equiv \int_{-\infty}^{+\infty} \varphi(x_0, y_0, z_0) dz_0 \tag{14}$$

that is related to the electrostatic potential. Finding the potential itself is impossible without making some additional assumptions about the potential variation along $z$.

The possibility of finding $\Phi$ stems from the form of expression (7) which, by taking account of Eq. (13), can be presented as a 2-dimensional Poisson equation for a "potential" $\Phi$:

$$\nabla^2 \Phi = -4\pi \mathrm{P}, \tag{15}$$

where a "charge density" P (upper-case rho) is expressed in terms of a measured intensity distribution:

$$\mathrm{P} = -\frac{W}{2e\pi}\left(\frac{I}{I_0} - 1\right) \tag{16}$$

Note that the integral of P over an area extending beyond the area occupied by perturbations is zero, so that there is no "net charge" corresponding to the r.h.s. of Eq. (16). This fact is clear from the structure of Eq. (15), which, if integrated over $\mathrm{d}x_0\mathrm{d}y_o$, would yield the derivatives of the deflection angles outside the perturbation area, these derivatives being zero together with the deflection angles themselves. With that notion in mind, one can write a standard 2D solution of the Poisson equation [Jackson? Smythe?]:

$$\Phi(\boldsymbol{r}_0) = 2\int P(\boldsymbol{r}_0') \ln\left(\frac{C}{|\boldsymbol{r}_0 - \boldsymbol{r}_0'|}\right) d^2\boldsymbol{r}_0', \tag{17}$$

where $\boldsymbol{r}$ and $\boldsymbol{r}'$ are two-dimensional vectors. The constant $C$ is an arbitrary constant: it drops out of the result, given the condition of the zero net charge. It is convenient to choose $C$ to be equal to a scale-length $a$ of the perturbations.

Another technique for solving Eq. (15) can be the use of a Fourier transform of Eq. (15). In both cases the background $I_0$ has to be corrected (for possible unrelated fluctuations and smooth variations) in such a way as to make the "net charge" zero, so that

$$I_0 = \frac{1}{S}\int I\, dS \tag{18}$$

where the integration is performed over the area that covers (with some margin) the intensity perturbation.

### C. Spherically-symmetric "blob"

#### *1. General equations*

Electrostatic perturbations are usually related to the ambipolar effects that maintain quasineutrality in a non-uniform plasma. If the electrons are strongly collisional and thereby Maxwellian, the potential variations are related to the density variations via the Boltzmann relation, $n \propto \exp(e\varphi / T_e)$. So, a positive potential would correspond to a density bump, whereas a negative potential would correspond to a density depression.

Accordingly, the presence of a localized density perturbation would manifest itself as a potential "blob" of a positive or negative sign.

A spherically-symmetric blob allows for a thorough analytical treatment and helps in identifying key effects in the formation of images. For this reason, we consider it in some detail.

For a spherically-symmetric perturbation, with $\varphi=\varphi(r)$, the deflection occurs in the plane passing through the unperturbed "ray" and the center of the sphere and can be characterized by a single angle $\alpha$, which depends on the impact parameter $r_0$, the distance between the center and the unperturbed ray. It is easy to show that the angular deflection in this case can be represented as

$$\alpha(r_0) = -\frac{4er_0}{W}\int_{r_0}^{\infty}\frac{dr}{\sqrt{r^2-r_0^2}}\frac{d\varphi}{dr}, \tag{19}$$

and the mapping to the image plane (in the limit $L>>l$) is given by

$$r = L\left(\frac{r_0}{l}+\alpha(r_0)\right) \tag{20}$$

For a focusing potential, $\alpha$ is negative, so that $r$ in Eq. (20) may formally become negative as well. This just means that the ray hits the image plane at the opposite side of the $z$ axis. In particular, if a caustic is formed at a formally negative $r$, its radius will be an absolute value of $r$ evaluated from Eq. (20).

As the surface element in the axisymmetric case is $dS = 2\pi r dr$, the intensity in the image plane will be

$$I = \frac{I^*}{\left|\frac{r}{r_0}\frac{dr}{dr_0}\right|+\varepsilon} \tag{21}$$

Equations (19)-(21) solve the imaging problem for a spherically-symmetric blob. We now consider two specific potential distributions: a Gaussian potential distribution and a flat-top distribution with sharp edges. The latter distribution may represent a two-scale potential (density) profile that may arise in the case of shocks with steep jumps in density (potential).

## 2. *A Gaussian "blob"*

Assume that the potential distribution is Gaussian,

$$\varphi = \varphi_0 \exp\left[-\frac{r_0^2}{a^2}\right]. \tag{22}$$

Performing the elementary integration in Eq. (19), we find that

$$\alpha = \frac{e\varphi_0}{W}\sqrt{\pi}\frac{r_0}{a}\exp\left[-\frac{r_0^2}{a^2}\right]. \tag{23}$$

An explicit expression for the derivative $dr/dr_0$ is

$$\frac{dr}{dr_0} = \frac{L}{l}\left(1+l\frac{d\alpha}{dr_0}\right) = \frac{L}{l}\left(1+\mu\left(1-2\frac{r_0^2}{a^2}\right)\exp\left(-\frac{r_0^2}{a^2}\right)\right), \tag{24}$$

where

$$\mu \equiv \sqrt{\pi}\,\frac{e\varphi_0}{W}\,\frac{l}{a} \quad . \tag{25}$$

Equation (25) is a quantitative analog of Eq. (6).

For $\mu \sim 1$ or $\mu > 1$, the intensity variations can be large and are given by combining Eqs. (21) and (24), as discussed in Appendix A. For $\mu << 1$, the intensity variations are weak, and an analog of Eq. (7) becomes:

$$\frac{I}{I_0} - 1 = -2\mu\left(1 - \frac{r_0^2}{a^2}\right)\exp\left(-\frac{r_0^2}{a^2}\right), \tag{26}$$

and $r_0 = rl/L$. For the focusing potential, the intensity in the central area, $r_0 < a$, increases, whereas the intensity at the periphery decreases. For the defocusing potential, the situation is opposite. Some examples of weak and strong focusing by spherical Gaussian blobs are shown in Fig. 3.

When $|\mu|$ increases, caustics are formed. According to Eq. (21), the position of the caustic corresponds to conditions of either $r$=0, or $dr/dr_0 = 0$. The first one corresponds to the less interesting solution of a point focus – a possibility characteristic of a purely spherical case. We therefore concentrate on the condition $dr/dr_0 = 0$. We then obtain from Eq. (24) the following equation for the radius of the caustic in the object plane:

$$1 + \mu\left(1 - 2\frac{r_0^2}{a^2}\right)\exp\left(-\frac{r_0^2}{a^2}\right) = 0\,. \tag{27}$$

The caustic appears at some critical value of the parameter $\mu$ (i.e., at some critical value of the potential $\varphi_0$). For the focusing (negative) potential the caustic appears at

$$\frac{e|\varphi_0|}{W} > \frac{a}{l\sqrt{\pi}} \approx 0.56\frac{a}{l}\,. \tag{28}$$

For the defocusing (positive) potential the caustic appears at

$$\frac{e\varphi_0}{W} > \frac{e^{3/2}}{2\sqrt{\pi}}\frac{a}{l} \approx 1.26\frac{a}{l}\,. \tag{29}$$

The position of the caustics in the object plane (Eq. (27)) vs. μ (the dimensionless potential) is presented in Fig. 5. The structure of the caustic in the image plane is considered in Appendix A.

As an example, we make numerical estimates for the case where $a$ = 0.3 mm, $l$=10 mm, and the proton beam energy W=10 MeV. We find that for the focusing potential the caustic would appear at $|\varphi_0|$>168 kV, whereas for the defocusing potential they appear at $\varphi_0$>378 keV. These potentials seem to be too high to be realistic in collisionless shock type experiments [Ross 2012, Park 2012, Loupias 2009, Gregory 2010, Kuramitsu 2011, Constantin 2009]. So, if caustics appear in the experiment, this may indicate formation of structures with sharp potential variation (like shock waves) that are discussed in the next sub-section.

### *3. Flat-top potential with sharp edges.*

The formation of step-wise potential distributions is possible in the presence of shock waves. We consider a model of a spherical structure which is flat inside a sphere of

a radius $a$ and then sharply changes to zero beyond this radius. In other word, the radial electric field will be present only in a narrow layer near $r_0=a$.

If one entirely neglects the structure of this transition, one finds a delta-function electric field, and Eq. (19) yields:

$$\alpha = \frac{4e\varphi_0}{W}\frac{r_0}{\sqrt{a^2-r_0^2}}, \quad r_0 < a$$
$$\alpha = 0, \quad r_0 > a \tag{30}$$

Here, obviously the radial derivative of $\alpha$ can be made arbitrary large near the blob surface. Actually, the finite width of a transition makes this derivative finite. An analysis of the effect of the final width is presented in Appendix A.

For comparison purposes, we introduce a parameter $\mu$ defined identically to Eq. (25). As was mentioned in Sec. IV.B2, it is small under realistic conditions. Therefore, $dr/dr_0=0$ can be satisfied only for the rays passing near the surface, at $\xi \equiv a-r_0 << a$. In this zone,

$$\alpha \approx \frac{2\sqrt{2}e\varphi_0}{W}\sqrt{\frac{a}{\xi}} = 2\mu\sqrt{\frac{2}{\pi}}\frac{a}{l}\sqrt{\frac{a}{\xi}} \tag{31}$$

## V. IMAGING OF MAGNETIC STRUCTURES

### A. General

The analysis that was presented in Sec. IV.A can be used almost directly to assess images of magnetic structures, with only a few modifications. The only assumption we make is that the field is weak enough, relative to the proton beam energy, to allow for the use of a perturbation technique associated with the integration of the perpendicular force along the unperturbed straight trajectory. [We should use uniform notations, say $x_0$, $y_0$ in the evaluation of deflection].

The direction of the unperturbed trajectory is $z$, with $x$ and $y$ being the transverse coordinates. One has:

$$\boldsymbol{F}_\perp = \frac{e}{c}\mathbf{v}\times\boldsymbol{B} \tag{32}$$

so that

$$\Delta\boldsymbol{p}_\perp = \frac{e}{c}\int_{-\infty}^{+\infty}[\mathbf{v}\times\boldsymbol{B}]dt \tag{33}$$

where the integration is carried out along the unperturbed trajectory.

Introducing the vector potential $\boldsymbol{A}$ of the magnetic field, one has

$$\boldsymbol{B} = \nabla\times\boldsymbol{A}\,. \tag{34}$$

For the field created by a localized system of currents, one can always choose the vector potential that would be zero at large distances from the current system [Landau 2008]. We will use this gauge below. One has (for a constant velocity $\mathbf{v}$)

$$\mathbf{v}\times\nabla\times\boldsymbol{A} = \nabla(\mathbf{v}\cdot\boldsymbol{A}) - (\mathbf{v}\cdot\nabla)\boldsymbol{A} \tag{35}$$

Integration over time is taken along the unperturbed trajectory, i.e., $x$ and $y$ are constant, and $dt=dz$/v. Substituting Eq. (35) in Eq. (33) and writing the $x$ component of the resulting equation (the $y$ component is treated analogously), one finds:

$$\Delta p_x = \frac{e}{c}\frac{\partial}{\partial x}\int_{-\infty}^{+\infty} A_z(x,y,z)dz - \frac{e}{c}\int_{-\infty}^{+\infty}\frac{\partial A_x(x,y,z)}{\partial z}dz \tag{36}$$

The latter integral is obviously zero for our gauge, so that we end up with results that are remarkably close, up to notation, to Eq. (13):

$$\alpha_x = \frac{e}{c\sqrt{2mW}}\frac{\partial}{\partial x}\int_{-\infty}^{+\infty} A_z(x,y,z)dz\,,\quad \alpha_y = \frac{e}{c\sqrt{2mW}}\frac{\partial}{\partial y}\int_{-\infty}^{+\infty} A_z(x,y,z)dz \tag{37}$$

They basically tell us that all the results of the previous calculations for electrostatic field can be used to evaluate the effect of magnetic perturbations by making the following substitution:

$$\varphi \to -\frac{\mathrm{v}}{c}A_z = -\sqrt{\frac{2W}{m}}\frac{1}{c}A_z \tag{38}$$

A key difference between electric and magnetic perturbations is the scaling of deflection with the proton energy $W$. Comparing Eqns. (37) and (13), we see that

$$\alpha_x \propto \frac{1}{W} \qquad \text{(electric)}, \qquad \alpha_x \propto \frac{1}{\sqrt{W}} \qquad \text{(magnetic)} \tag{39}$$

This difference can be used to distinguish between electric and magnetic perturbations, especially for experiments with polyenergetic proton beams that yield multiple radiographs at different proton energies [Roth 2011].

For a magnetic perturbation of a single scale $a$, one has $A\sim aB$, so that a deflection angle evaluated from Eq. (37) is $\alpha\sim a/\rho_P$ , where $\rho_P$ is a proton beam gyro-radius in a field $B$. Then, the condition for the caustics formation $\mu>1$, with $\mu$ defined by Eq. (6), becomes, by an order of magnitude, $\rho_P > l$. For $l\sim 1$ cm and $W\sim 10$ MeV this requires a magnetic field exceeding 0.5 MG.

The inversion procedures discussed in Sec. IV.B can be directly applied to magnetic perturbations, with the substitute (38). If both electrostatic and magnetostatic perturbations are present, the inversion would recover an integral

$$\tilde{\Phi}(x_0,y_0) \equiv \int_{-\infty}^{+\infty}\left[\varphi(x_0,y_0,z_0) - \frac{\mathrm{v}}{c}A_z(x_0,y_0,z_0)\right]dz_0\,. \tag{40}$$

Our analysis in this paper focuses on static perturbations. In Section VII below we discuss the effect of slow time-variations that might cause some "blurring" of the images. Another effect of the time variation is that it may produce a vortex component of the electric field. Here we assess conditions under which such an effect is subdominant and can be ignored. The vortex electric field can be evaluated as $E_{vort} \sim (a/c\tau)B$, where $\tau$ is the characteristic time of the magnetic field variation, and $a$ is the spatial scale of magnetic and electric features. One can compare this field with an electrostatic, curl-free component, which is $\sim\varphi/a$. The second is much greater than the first if $\tau >> a^2B/c\varphi$ . The electrostatic potential typically scales as an electron temperature, $\varphi \sim T_e/e$ . Our criterion then becomes:

$$\tau >> a^2/(cT_e/eB) \tag{41}$$

Interestingly, the factor in the denominator is a Bohm diffusion coefficient (without a 1/16 factor). Numerically, Eq. (41) reads as $\tau(ps) > [a(\mu m)]^2 B(T)/T_e(eV)$. For $B$=10 T, $a$=100 μm, and $T_e$=1 keV the constraint is $\tau$>100 ps. For a weaker magnetic field, a much faster evolution is allowed.

### B. Imaging the magnetic field of current filaments

In some models of electromagnetic instabilities in counterstreaming plasmas [Kato 2008, Medvedev 1999, Moiseev 1963], current filaments parallel to the direction of the streams are expected to be formed. It turns out that such structures do not produce any substantial deflection of the beam in the linear approximation that we have used thus far. Indeed, the straight current filament produces a field that has only an azimuthal component. The beam crossing this field structure along a straight line (an approximation used to evaluate the acquired momentum) experiences mutually compensating kicks in whatever direction it crosses the filament. So, the deflection in this approximation becomes zero. The net deflection may appear due to the deviation of the filament from a straight line, or due to the variation of the filament thickness along its axis, or due to non-linear terms (i.e., with the account of the deviation of the proton trajectory from an unperturbed straight line). The former effect is considered in Appendix D, whereas the latter effect is evaluated in the next section.

## VI HIGHER-ORDER CORRECTIONS

In the previous sections, we evaluated the angular deflection to the lowest order in the parameters $a/l$ (the paraxiality) and $\alpha$ (deflection angle). Although both are small under the conditions of the experiments discussed earlier, it is worthwhile to evaluate second-order corrections in order to have a better understanding of the applicability conditions.

We characterize a particular ray by the coordinates $x_0$, $y_0$ of its intersection with the object plane in the absence of the perturbation. In the presence of the perturbation, the ray that leaves the interaction zone in the vicinity of the object plane is a straight line, whose direction has changed with respect to the unperturbed one and whose intersection with the object plane has changed with respect to $x_0$, $y_0$ , (Fig. 6) and became some $x'_0$, $y'_0$.

To perform further analysis, it is convenient to make a coordinate frame transformation. By rotating the frame around the axis $z$ (Fig. 1) one can always make $y_0$=0, so that the initial ray would lie in the ($x$,$z$) plane. After that, by shifting the frame along axis $x$ and rotating it around the axis $y$, one can make the axis $z$ to coincide with the direction of the unperturbed beam (Fig. 6). We will denote the coordinates in this new frame as $\xi$ (for $x$), $\eta$ (for $y$) and $\zeta$ (for $z$). As mentioned, the coordinate $\zeta$ is directed along the unperturbed beamlet. The transformation from the new frame to the old one reads as:

$$x = \frac{\xi l + \zeta x_0}{\sqrt{x_0^2 + l^2}} + x_0;$$
$$y = \eta; \qquad (42)$$
$$z = \frac{-\xi x_0 + \zeta l}{\sqrt{x_0^2 + l^2}}.$$

In this frame, the protons approach an object (a plasma) along a line $\xi = 0, \eta = 0$, with a velocity $v_0$ directed along the axis $\zeta$. The electric field in the new frame is localized near $\zeta$=0, so that the protons experience the effect of the electric field only in this narrow zone. The electric field is a function of $\xi, \eta, \zeta$ : $E_\xi(\xi,\eta,\zeta) = -\partial\varphi(\xi,\eta,\zeta)/\partial\xi$, and analogously for the other two components. In the course of interaction with the electric field, the protons deviate from the initial straight line.

Calculations of the proton trajectory up to the terms of the second order in the electric field, without an assumption of the paraxiality, is presented in Appendix E. The final results for the position of the proton intersection with the image plane reads as

$$x = x_0 + L\frac{l\tan\alpha_x + x_0}{l - x_0\tan\alpha_x}, \qquad (43)$$

where the parameter $\tan\alpha_x$ is given by Eq. (E10). The displacement along the $y$ axis is evaluated analogously. With the second-order terms omitted, one recovers Eq. (1). Equation (43) generalizes Eq. (1') in two respects: there is no assumption of the paraxiality, and the second-order terms are retained in the expression for $\alpha$. Assuming $x_0 << l$ and $\alpha_x << 1$, one recovers Eq. (1').

## VII. SPATIAL RESOLUTION

The spatial resolution of the images depends on several factors: the finite resolution of the radiochromic film used to reveal the images, the finite source brightness, and temporal variation of the object. Discussing the properties of the film goes well beyond the scope of this paper; we will focus therefore on the limitations caused by the temporal effects and finite source brightness. We will limit ourselves to the practically most important case of modest density variations (no caustics), which is adequately described by Eqs. (7), (8).

The proton beam traverses the object of a scale $a$ within the time $a/v$. The images produced by protons of varying energy are separated in time by the time-of-flight stretching on the way from the source to the object. For the relative velocity variation over the pulse, $\eta = \Delta v / v$, the time between the fastest and the slowest particles to reach the object is $\eta l / v$. For the beam velocity of $4\times10^9$ cm/s, $l$=1 cm, and $\eta$=0.3 this time is ~ 75 ps. In other words, if the shape of the object changes significantly over the time shorter than 75 ps, the faster and slower protons probe essentially different objects. This effect is often used for the assessment of the time evolution of the object [Roth 2011], if the energy bins in the detection system are much narrower than the $2\eta W$, where $W$ is an average beam energy. Note that the further temporal spreading of the proton pulse on the segment $L$ of its trajectory does not affect the image, as the proton beam at this segment propagates ballistically and does not change its energy or angular distributions.

In this discussion we assumed that the proton pulse is produced within a time that is shorter than the time-of-flight dispersion, $\eta l / \mathrm{v}$. Under conditions of a typical radiography experiment the generation time is indeed shorter, on the order of the laser pulse length (10 ps to less than 1 ps).

Consider now an effect of a finite source size, or, more generally, an effect of a non-zero phase-space volume occupied by the beam. In our earlier assessment we assumed that the beam is produced in a point source, with a smooth angular distribution over the angle within the field of view. The latter assumption is important, as otherwise, even in the absence of any perturbing object, the intensity distribution in the image plane would be spotty.

To imitate the finite source size, we consider an image produced by the identical source but displaced tangentially by a distance $\xi$ with respect to the first one. This would obviously cause the displacement of the image by the distance $\xi L/l$. On the other hand, the size of the image is $aL/l$, where $a$ is the size of the object. So, in order to resolve an object of a size $a$, one has to have a source of the size $\xi << a$. If the object contains features of different spatial scales, $\xi$ has to be smaller than the smallest feature. Stated in terms of the angular source size $\theta = a/l$, we must have $\xi << \theta l$

In this discussion we tacitly assumed that each piece of a finite-size source produces a divergent stream of the protons. This is true for the imploding $D^3He$ pellet [Li 2010], but may not necessarily be the case for the electrostatically-accelerated protons. In the latter case, the shape of the plasma cloud from which the protons are extracted will affect the angular distribution. The shape can be defocusing or focusing, this producing an equivalent source situated either further from or nearer to the object (Fig. 1). It seems that the former option has been realized in some of the experiments [Borghesi 2004], this meaning that the parameter $l$ may be somewhat larger than the nominal distance between the proton target and the object. In the experiment described in [Borghesi 2004], the proton emission area of roughly 100 μm diameter was inferred to be equivalent to a much smaller (~5 μm diameter) virtual source originating approximately 0.5 mm farther away from the object that was being imaged.

## VIII. SUMMARY AND DISCUSSION

Our study has been focused on the practically most important systems with a large magnification, $L>>l$. In such systems, the main contribution to the position of the ray on the image plane is determined by the deflection angle $\alpha$: the displacement of the ray in the image plane scales as $\alpha L$ and grows linearly with $L$. Conversely, the shift of the ray on its way through the perturbation does not depend on $L$. This leads to significant simplification of the projection equations.

As shown in this paper, there exist two very different regimes of the proton imaging: that of a small deflection, when the intensity variations are modest, below 25-30 percent compared to the average intensity, and that of a stronger deflection, where the caustics are formed, and intensity variations can be in the factors of 10 and more. The transition from the first to the second regime occurs at characteristic deflection angles $\sim a/l$, where $a$ is the size of a feature and $l$ is the distance between the proton source and the object.

Note that, for a practically important case of $a<<l$, the deflection angles corresponding to the caustic formation are small, so that the analytic "machinery" developed in Sec. II – III for the evaluation of the deflection angle and based on the paraxial approximation still works. A remarkable feature of a model of small deflection in a paraxial system is that it establishes a simple correspondence between the deflection caused by electrostatic and magnetostatic fields (Sec. V A).

The case of small intensity variations (far from formation of caustics) is interesting in that it allows for a simple reconstruction of the line-integrated potential (or vector potential) from the radiographic image (Sec. IV B).

For an object with a smooth distribution of the electric field, which can be characterized by a single spatial scale $a$, the transition to the caustic regime corresponds to the electrostatic potential of order $(W/e)(a/l)$, where $W$ is the proton energy. For $a/l$~1/30, and the proton energy of 10 MeV, this corresponds to quite high potential variations in a plasma, ~300 kV. If, on the other hand, there exists a potential distribution with sharp transitions of a small scale (e.g., shock waves) then caustics can be generated by much smaller potentials.

For the magnetic field structures of a scale $a$, the caustics are formed at the magnetic field for which $\rho_P < l$, where $\rho_P < l$ is a proton gyro-radius for this field. For a 10 MeV probe beam and the distance $l$ of 1 cm, this corresponds to a field of 0.5 MG. A significant difference with respect to the electrostatic case appears in the effect of shock waves. The ambipolar electric field on the shock front is determined by the quasineutrality constraint, and the electrostatic potential varies in concert with the density. So, the density jump leads to a potential jump, whence to a very high electric field within the front. Conversely, a shock propagating in the magnetic field produces a jump in the magnetic field strength, not a narrow (delta-function-like) peak of the field. So, a magnetic shock structure wouldn't necessarily generate caustics by the same mechanism as the one that is at work in an ambipolar electric field.

The spatial resolution of the images, aside from the resolution of the radiochromic film, is determined by the effective size of the proton source and temporal variation of both the object and the source (Sec. VII).

**Acknowledgements.**

We thank the following individuals for helpful discussions and other contributions to our understanding of proton imaging: Anatoly Spitkovsky and Luis Gargate of Princeton University; Scott Wilks, Claudio Bellei, Andy MacKinnon, Prav Patel, and Bruce Remington of LLNL; Philip Nilson of the Laboratory for Laser Energetics; Radu Presura of the University of Nevada, Reno; Mingsheng Wei of General Atomics; Louise Willingale of the University of Michigan; Mario Manuel and Chikang Li of the Massachusetts Institute of Technology. This work was performed under the auspices of the U.S. Department of Energy by Lawrence Livermore National Security, LLC, Lawrence Livermore National Laboratory, under Contract DE-AC52-07NA27344. Additional support was provided by LLNL LDRD Grant No. 11-ERD-054.

## Appendix A. Caustics for a spherically-symmetric Gaussian blob

It is instructive to relate the radius of the caustic in the image plane and the size of the blob *a*. One has from Eqs. (20), (23) and (27):

$$r = r_0 \frac{L}{l}\left|1+\mu\exp\left(-\frac{r_0^2}{a^2}\right)\right| = r_0 \frac{L}{l}\left|\frac{2(r_0^2/a^2)}{2(r_0^2/a^2)-1}\right|, \qquad (A.1)$$

where we have used Eq. (27) to express $\mu$ in terms of a caustic radius in the image plane. We introduced an absolute value sign per discussion after Eq. (20). Eqs. (A.1) and (27) provide a parametric representation for the dependence $r(\mu)$, with $r_0$ being a parameter. Instead of *r*, one can plot the ratio *r/a*. This parameter depends on $\mu$ and is different from the parameter *L/l*, which characterizes magnification for the contrast imaging. The plot of the ratio of the two,

$$(r/a)(l/L) \equiv M \qquad (A.2)$$

is shown in Fig. 7 as a function of the dimensionless potential μ. Proton images produced by spherically symmetric Gaussian blobs are shown in Fig. 3.

For the defocusing potential, the parameter M is close to 2 in a relatively broad range of parameters. This means that the size of the object is roughly 2 times smaller than a simple estimate $a=rl/L$. For the focusing potential, the situation is more complex: the object can be both larger and smaller than an estimate $a=rl/L$. What could help in the interpreting the image, is the dependence of the image size on the proton energy: changing the energy *W* changes the parameter μ without changing *a* and $\varphi_0$.

A feature of Eq. (A.1) which may seem paradoxical is the divergence at $r_0 = a/\sqrt{2}$. In fact, this feature just shows that, for a very large value of the potential, such that $|\mu|>>1$, one of the caustics has to be situated near the radius $r_0 = a/\sqrt{2}$, which corresponds to a zero derivative $d\alpha/dr_0$. At a large value of potential, the deflection angle is large leading to large r in the image plane. Therefore, there is a singularity in the dependence of *r* vs $r_0$ at $r_0 = a/\sqrt{2}$. The presence of the singularity just tells us that, to have a caustic at $r_0 \approx a/\sqrt{2}$, one has to have a very high potential and, respectively, a very high deflection angle.

The intensity in the image plane is determined by Eq. (21) which, according to Eqs. (20), (23) and (24) can be rewritten as:

$$I = \frac{I_0}{\left(\frac{L}{l}\right)^2\left|\left[1+\mu\left(1-2\frac{r_0^2}{a^2}\right)\exp\left(-\frac{r_0^2}{a^2}\right)\right]\left(1+\mu\exp\left(-\frac{r_0^2}{a^2}\right)\right)\right| + \varepsilon} \qquad (A.3)$$

Equations (A.1) and (A.3) provide a parametric representation of the intensity distribution in the image plane $I(r)$. A characteristic intensity distribution in the image plane for μ=1 (defocusing) is shown in Fig. 8.

## Appendix B. A spherical potential "blob" with a sharp edge

Here we consider the same problem as that discussed in Sec. IV.C.3, but with account for the final width of a blob boundary. Specifically, instead of using a delta-function distribution of the electric field, as in Sec. IV.C.3, we now assume that near the boundary

$$E_r = \frac{\varphi_0 h}{\pi\left[\left(r_0 - a\right)^2 + h^2\right]} \tag{B.1}$$

with $h<<a$. In the vicinity of the boundary, at $|r_0 - a| << a$, by making an approximation $r^2 - r_0^2 \approx 2a(r - r_0)$ one can obtain the following expression for the deflection angle:

$$\alpha(r_0 - a) = \frac{2ea\varphi_0}{W\sqrt{2ah}} F\left(\frac{r_0 - a}{h}\right) \tag{B.2}$$

where $F$ is the following dimensionless function of a dimensionless argument:

$$F(\xi) = \frac{2}{\pi}\int_{-\infty}^{\infty} \frac{d\eta}{\left(\eta^2 + \xi\right)^2 + 1} \tag{B.3}$$

Switching to integration in a complex plane $\eta$, one notices that there are two first-order zeros of the denominator in the upper half plane. Closing the integration contour in the upper half-plane and taking residues in these two poles, one finds:

$$F(\xi) = \frac{\sqrt{\sqrt{\xi^2 + 1} - \xi}}{\sqrt{\xi^2 + 1}} \tag{B.4}$$

The plot of this function and its derivative is given in Fig. 9. The derivative has two extrema that correspond to the first appearance of the caustic when the absolute value of the potential in the blob increases. In the focusing case ($\varphi_0<0$) the caustic appears at $\xi$=-1.25 and in the defocusing case ($\varphi_0>0$) at $\xi$=0.3. The required potential amplitude is

$$\frac{e\varphi_0}{W} > 3.7\frac{\sqrt{ah}}{l} \tag{B.5}$$

and

$$\frac{e|\varphi_0|}{W} > 1.1\frac{\sqrt{ah}}{l}, \tag{B.6}$$

respectively. If $h$ is significantly smaller than the global scale $a$ of the perturbation, the caustics would appear at a smaller value of the potential than for a smooth "blob" (Eq. (27)). This can be the case if h is a shock thickness or a Debye sheath thickness.

Of interest is also a characteristic intensity distribution in the case of a small potential, when the caustics are not present and one can use Eq. (7). The distribution has a characteristic shape. For a focusing potential, intensity is higher inside the blob, and a narrow ring with a much lower intensity is formed around the blob. In the defocusing case, the situation is opposite.

## Appendix C. An ellipsoidal Gaussian "blob"

We consider a Gaussian potential distribution, with equipotentials being nested ellipsoids. If the ellipsoid axis coincides with axis $z$, this distribution can be presented as

$$\varphi = \varphi_0 \exp\left(-\frac{x_0^2 + y_0^2}{a^2} - \frac{z_0^2}{b^2}\right). \tag{C.1}$$

One can also account for a possible tilt of the ellipsoid with respect to the axis $z$, as shown in Fig. 2. The tilting by an angle $\theta$ is achieved by turning the system around the axis $x$ by that angle: $x_0 \rightarrow x_0$, $y_0 \rightarrow y_0 \cos\theta - z_0 \sin\theta$, $z_0 \rightarrow y_0 \sin\theta + z_0 \cos\theta$. The potential distribution then becomes

$$\varphi = \varphi_0 \exp\left[-\frac{x_0^2}{a^2} - \frac{y_0^2}{d^2}\right] \exp\left[-z_1^2 \frac{d^2}{a^2 b^2}\right], \tag{C.2}$$

$$z_1 = z_0 + y_0 \sin\vartheta \cos\vartheta \frac{\left(b^2 - a^2\right)}{d^2}, \tag{C.3}$$

$$d \equiv \sqrt{a^2 \cos^2\vartheta + b^2 \sin^2\vartheta}\,. \tag{C.4}$$

Here $\varphi$ has been put in a form that will permit the convenient integration of Eq. (10) via table lookup.

Performing the standard integration over $z_1$ (related to $z_0$ by Eq. (13)) one finds:

$$\int_{-\infty}^{+\infty} \varphi(x_0, y_0, z_0) dz_0 = \varphi_0 \frac{ab\sqrt{\pi}}{d} \exp\left[-\frac{x_0^2}{a^2} - \frac{y_0^2}{d^2}\right], \tag{C.5}$$

so that

$$\alpha_x = f \frac{x_0}{a^2} d\,, \tag{C.6}$$

$$\alpha_y = f \frac{y_0}{d}\,, \tag{C.7}$$

$$f(x_0, y_0) = \frac{e\varphi_0}{W} \frac{ab\sqrt{\pi}}{d^2} \exp\left[-\frac{x_0^2}{a^2} - \frac{y_0^2}{d^2}\right]. \tag{C.8}$$

The derivatives that enter Eq. (6) can be presented as:

$$\frac{\partial \alpha_x}{\partial x_0} = \frac{fd}{a^2}\left(1 - \frac{2x_0^2}{a^2}\right);\ \frac{\partial \alpha_y}{\partial y_0} = \frac{f}{d}\left(1 - \frac{2y_0^2}{d^2}\right); \tag{C.9}$$

$$\frac{\partial \alpha_x}{\partial y_0} = \frac{\partial \alpha_y}{\partial x_0} = -\frac{2x_0 y_0 f}{a^2 d}\,. \tag{C.10}$$

Consider the case of a small intensity variation (small deflection angles). Equation (7) yields:

$$\frac{I}{I_0} - 1 = -\frac{fld}{a^2}\left[\left(1 - \frac{2x_0^2}{a^2}\right) + \frac{a^2}{d^2}\left(1 - \frac{2y_0^2}{d^2}\right)\right], \tag{C.11}$$

where $x_0$ and $y_0$ have to be expressed in terms of $x$, $y$ (the coordinates in the image plane) by Eqns. (8). One sees that for the positive (defocusing) potential blob, the intensity decreases near the center of the image and increases at the periphery, before returning to the unperturbed level at infinity. For the negative (focusing) perturbation the situation is opposite. Equation (5) gives us the intensity in the image plane:

$$I = \frac{I_0}{\left|1 + \frac{fld}{a^2}\left[\left(1 - \frac{2x_0^2}{a^2}\right) + \frac{a^2}{d^2}\left(1 - \frac{2y_0^2}{d^2}\right)\right] + \left(\frac{fld}{a^2}\right)^2 \left(1 - \frac{2x_0^2}{a^2} - \frac{2y_0^2}{d^2}\right)\right| + \varepsilon} \qquad \text{(C.12)}$$

Fig. 3 shows Eq. C.12 plotted (with the technique described in Appendix F) for several values of positive and negative $\mu$.

Long, filamentary potential perturbations correspond to $b>>a$. The perturbations in this case can become essentially one-dimensional, as shown in Fig. 10.

Using Equations (5'), (9), (C.9) and (C.10), one finds the following equation for the caustics for the ellipsoidal blob:

$$1 + \frac{fld}{a^2}\left[\left(1 - \frac{2x_0^2}{a^2}\right) + \frac{a^2}{d^2}\left(1 - \frac{2y_0^2}{d^2}\right)\right] + \left(\frac{fld}{a^2}\right)^2 \left(1 - \frac{2x_0^2}{a^2} - \frac{2y_0^2}{d^2}\right) = 0\,. \qquad \text{(C.13)}$$

Several characteristic shapes of the caustic curves at the object plane are shown (in the units of $a$) in Fig. 11, for various ratios of $d/a$. Note that even one, very simple object, a spherical potential well, can produce two caustics. Note also the appearance of characteristic cusps (self- intersections) in some cases. The tilting of the deflecting potential structure in the plane of a figure would produce tilted images.

Caustics are formed for the defocusing potentials as well—they just require higher potential for their formation. A couple of examples of the caustics produced by the defocusing potential are shown in Fig. 12.

## Appendix D. An ellipsoidal magnetic "blob"

Here we present a model magnetic field structure that represents a Gaussian "blob" of a magnetic field as shown in Fig. 13. We consider an axisymmetric structure and describe it in cylindrical coordinates with an axis z' coinciding with rotation axis. We use "primes" here to distinguish these coordinates from the ones in Section II, where the axis $z$ was chosen to coincide with the direction of a probe beam proton. We later allow for arbitrary tilts of the "blob" axis, which (tilting) can be accomplished by a simple coordinate transformation.

The magnetic field has a $\varphi'$ component, whereas the current that generates it has $z'$ and $r'$ components:

$$B_{\varphi'} = B_0 \frac{r'}{a} \exp\left(-\frac{r'^2}{a^2} - \frac{z'^2}{b^2}\right) \qquad \text{(D.1)}$$

$$j_{r'} = \frac{cr'z'}{2\pi a b^2} \exp\left(-\frac{r'^2}{a^2} - \frac{z'^2}{b^2}\right) \qquad \text{(D.2)}$$

$$j_{z'} = \frac{c}{2\pi a}\left(1 - \frac{r'^2}{a^2}\right) \exp\left(-\frac{r'^2}{a^2} - \frac{z'^2}{b^2}\right) \qquad \text{(D.3)}$$

The current streamlines are defined by the equation

$$r'^2 \exp\left(-\frac{r'^2}{a^2}-\frac{z'^2}{b^2}\right)=const \tag{D.4}$$

and are shown in Fig. 13 . The vector potential for this field can be chosen as

$$A_{z'}=\frac{B_0 a}{2}\exp\left(-\frac{r'^2}{a^2}-\frac{z'^2}{b^2}\right),\quad A_{\varphi'}=A_{r'}=0 \tag{D.5}$$

The vector potential can also be written in a Cartesian "primed" system:

$$A_{z'}=\frac{B_0 a}{2}\exp\left(-\frac{x'^2+y'^2}{a^2}-\frac{z'^2}{b^2}\right),\quad A_{x'}=A_{y'}=0 \tag{D.6}$$

Now we perform the transformation of tilting the axis in the y-z plane of Fig. 1. The tilt in the xy plane will lead to a trivial effect of turning the image around the probe beam axis. The tilt angle will be denoted by γ and will be measured from the direction of the probe beam. In other words, $\gamma$=0 corresponds to the blob axis aligned with the probe beam, whereas $\gamma=\pi/2$ corresponds to the blob axis normal to the beam. One has:

$$\begin{aligned} x' &= x \\ y' &= y\cos\gamma - z\sin\gamma \\ z' &= y\sin\gamma + z\cos\gamma \end{aligned} \tag{D.7}$$

and

$$\begin{aligned} A_x &= A_{x'}=0 \\ A_y &= A_{y'}\cos\gamma + A_{z'}\sin\gamma = A_{z'}\sin\gamma \\ A_z &= -A_{y'}\sin\gamma + A_{z'}\cos\gamma = A_{z'}\cos\gamma \end{aligned} \tag{D.8}$$

According to Sec. B, we need only the z component of the vector potential in our "master" frame of Fig. 1. Substituting Eqs.(D.7) into Eq. (D.6) and using the last of Eqs. (D.8), we find

$$A_z=\frac{B_0 a\cos\gamma}{2}\exp\left(-\frac{x'^2+y'^2}{a^2}-\frac{z'^2}{b^2}\right)=\frac{B_0 a\cos\gamma}{2}\exp\left(-Q\right) \tag{D.9}$$

where

$$Q\equiv\frac{x^2}{a^2}+y^2\left(\frac{\cos^2\gamma}{a^2}+\frac{\sin^2\gamma}{b^2}\right)-2yz\sin\gamma\cos\gamma\left(\frac{1}{a^2}-\frac{1}{b^2}\right)+z^2\left(\frac{\sin^2\gamma}{a^2}+\frac{\cos^2\gamma}{b^2}\right) \tag{D.10}$$

Having in mind that, according to Eq. (37), we have to perform an integration over $z$, it is convenient to represent $Q$ in the equivalent form:

$$Q=\frac{x^2}{a^2}+\frac{y^2}{d^2}+z_1^2\frac{d^2}{a^2b^2}, \tag{D.11}$$

$$z_1=z+y\sin\gamma\cos\gamma\frac{\left(b^2-a^2\right)}{d^2}, \tag{D.12}$$

$$d\equiv\sqrt{a^2\cos^2\gamma+b^2\sin^2\gamma}\,. \tag{D.13}$$

Performing an elementary integration over dz, one recovers Eqs. (C.9)-(C.12), with the only difference that $f$ now is defined as:

$$f(x_0,y_0)=\frac{eB_0a\cos\gamma}{cM\mathrm{v}}\frac{ab\sqrt{\pi}}{d^2}\exp\left[-\frac{x_0^2}{a^2}-\frac{y_0^2}{d^2}\right] \tag{D.14}$$

## Appendix E. Evaluating the higher-order corrections.

To find an angular deflection of the protons after their traversal of the object, one has to iteratively solve a set of equations

$$\delta\ddot{\xi}=a_\xi(\xi,\eta,\zeta), \tag{E.1}$$

etc., where

$$\boldsymbol{a}=(e/m_p)\boldsymbol{E}, \tag{E.2}$$

and the right hand side is evaluated for the instantaneous positions of the proton, $\xi(t),\eta(t),\zeta(t)$. Since the position along $\zeta$ and the $\zeta$ component of the velocity are single-valued functions of time, one can equivalently characterize the r.h.s. of Eq. (42) in terms of coordinate $\zeta$ related to the time by

$$\frac{d\zeta}{dt}=\mathrm{v}_\zeta(\zeta). \tag{E.3}$$

Then one has (exactly):

$$\begin{aligned}
\mathrm{v}_\xi(\zeta)&=\int_{-\infty}^{\zeta}a_\xi\left[\xi(\zeta),\eta(\zeta),\zeta\right]\frac{d\zeta}{\mathrm{v}_\zeta(\zeta)};\\
\mathrm{v}_\eta(\zeta)&=\int_{-\infty}^{\zeta}a_\eta\left[\xi(\zeta),\eta(\zeta),\zeta\right]\frac{d\zeta}{\mathrm{v}_\zeta(\zeta)};\\
\mathrm{v}_\zeta(\zeta)&=\mathrm{v}_0+\int_{-\infty}^{\zeta}a_\zeta\left[\xi(\zeta),\eta(\zeta),\zeta\right]\frac{d\zeta}{\mathrm{v}_\zeta(\zeta)}.
\end{aligned} \tag{E.4}$$

Now we start iterations, assuming that the velocity variation is small compared to $\mathrm{v}_0$. In the zeroth-order approximation, one has $\xi^{(0)}=\eta^{(0)}=0$, $\mathrm{v}_\xi^{(0)}=\mathrm{v}_\eta^{(0)}=0$, $\mathrm{v}_\zeta^{(0)}=\mathrm{v}_0$. The first-order velocity perturbation is found by substituting the zeroth-order solution to the r.h.s. of Eq. (E.4):

$$\begin{aligned}
\mathrm{v}_\xi^{(1)}(\zeta)&=\int_{-\infty}^{\zeta}a_\xi\left[0,0,\zeta\right]\frac{d\zeta}{\mathrm{v}_0};\\
\mathrm{v}_\eta^{(1)}(\zeta)&=\int_{-\infty}^{\zeta}a_\eta\left[0,0,\zeta\right]\frac{d\zeta}{\mathrm{v}_0};\\
\mathrm{v}_\zeta^{(1)}(\zeta)&=\int_{-\infty}^{\zeta}a_\zeta\left[0,0,\zeta\right]\frac{d\zeta}{\mathrm{v}_0}.
\end{aligned} \tag{E.5}$$

The point $\xi=0,\ \eta=0$ corresponds to the point $x_0,\ y_0$ of the initial coordinate frame.

By performing one more integration, one finds the first-order displacement:

$$\xi^{(1)}(\zeta)=\int_{-\infty}^{\zeta}d\xi\int_{-\infty}^{\zeta'}a_{\xi}\left[0,0,\zeta'\right]\frac{d\zeta'}{\mathrm{v}_0};$$
$$\eta^{(1)}(\zeta)=\int_{-\infty}^{\zeta}d\xi\int_{-\infty}^{\zeta'}a_{\eta}\left[0,0,\zeta'\right]\frac{d\zeta'}{\mathrm{v}_0}. \tag{E.6}$$

Second-order velocity perturbations are:

$$\mathrm{v}_{\xi}^{(2)}(\zeta)=\int_{-\infty}^{\zeta}\left[\xi^{(1)}(\zeta)\frac{\partial a_{\xi}(0,0,\zeta)}{\partial\xi}+\eta^{(1)}(\zeta)\frac{\partial a_{\xi}(0,0,\zeta)}{\partial\eta}-a_{\xi}(0,0,\zeta)\frac{\mathrm{v}_{\xi}^{(1)}(\zeta)}{\mathrm{v}_0}\right]\frac{d\xi}{\mathrm{v}_0};$$
$$\mathrm{v}_{\eta}^{(2)}(\zeta)=\int_{-\infty}^{\zeta}\left[\xi^{(1)}(\zeta)\frac{\partial a_{\eta}(0,0,\zeta)}{\partial\xi}+\eta^{(1)}(\zeta)\frac{\partial a_{\eta}(0,0,\zeta)}{\partial\eta}-a_{\eta}(0,0,\zeta)\frac{\mathrm{v}_{\xi}^{(1)}(\zeta)}{\mathrm{v}_0}\right]\frac{d\xi}{\mathrm{v}_0}; \tag{E.7}$$
$$\mathrm{v}_{\zeta}^{(2)}(\zeta)=\int_{-\infty}^{\zeta}\left[\xi^{(1)}(\zeta)\frac{\partial a_{\zeta}(0,0,\zeta)}{\partial\xi}+\eta^{(1)}(\zeta)\frac{\partial a_{\zeta}(0,0,\zeta)}{\partial\eta}-a_{\zeta}(0,0,\zeta)\frac{\mathrm{v}_{\xi}^{(1)}(\zeta)}{\mathrm{v}_0}\right]\frac{d\xi}{\mathrm{v}_0}.$$

To find the displacement in the $\xi,\eta$ plane (i.e., in the direction perpendicular to that of the initial beamlet), one has to perform one more integration. For example, for $\xi$ up to the terms of the second order, one has (Cf. Eqs. (E.5) and (E.6)):

$$\xi\approx\xi^{(1)}+\xi^{(2)}=\int_{-\infty}^{\zeta}d\zeta'\int_{-\infty}^{\zeta'}Q_{\xi}d\zeta'' \tag{E.7}$$

where

$$Q_{\xi}(\zeta)=\frac{1}{\mathrm{v}_0^2}\left[a_{\xi}\left(0,0,\zeta\right)+\xi^{(1)}(\zeta)\frac{\partial a_{\xi}(0,0,\zeta)}{\partial\xi}+\eta^{(1)}(\zeta)\frac{\partial a_{\xi}(0,0,\zeta)}{\partial\eta}-a_{\xi}(0,0,\zeta)\frac{\mathrm{v}_{\xi}^{(1)}(\zeta)}{\mathrm{v}_0}\right]. \tag{E.8}$$

An expression in the square brackets is zero in the zone outside the plasma, i.e., at large $|\zeta|$. Using this circumstance and integrating by parts in Eq. (E.7), one finds that outside the interaction zone

$$\xi(\zeta)\approx\xi^{(1)}+\xi^{(2)}=\zeta\int_{-\infty}^{\infty}Q_{\xi}(\zeta')d\zeta'-\int_{-\infty}^{\infty}\zeta'Q_{\xi}(\zeta')d\zeta' \tag{E.9}$$

This is a very helpful representation of the perpendicular displacement, as it separates, in a formal way, the contribution related to the tilt of the beam (the first term, growing linearly with the distance) and a constant displacement that occurs during the beam transit through the plasma. Both are generally present, but for $L>>a$ (as is the case in real situations), the second term is very small compared to the first one ($\sim a/L$, unless some improbable cancellations make the first term zero). It is natural to use a notation $\tan\alpha_x$ to designate an integral in the first term, although now, compared to Sec. II, it contains second-order effects and is not based on the paraxial approximation:

$$\tan\alpha_x=\int_{-\infty}^{\infty}Q_{\xi}(\zeta')d\zeta'. \tag{E.10}$$

Taking into account this circumstance and neglecting the last term, we see that, according to Eq. (42), the intersection of the beamlet with the image plane occurs at

$$\zeta=\frac{L\sqrt{l^2+x_0^2}}{l-x_0\alpha_x}. \tag{E.11}$$

At this point, according to Eq. (E.9), with the last term neglected,

$$\xi = \zeta \tan\alpha_x = \frac{L\sqrt{l^2 + x_0^2}}{l - x_0 \tan\alpha_x} \tan\alpha_x \,, \tag{E.12}$$

so that, according to Eq. (42), the coordinate $x$ of the intersection point is:

$$x = x_0 + L\frac{l\tan\alpha_x + x_0}{l - x_0\tan\alpha_x} \,. \tag{E.13}$$

**Appendix F. Procedure for generating synthetic proton images**

The images shown in Figures 3, 4, 10, and 11 were made using the following technique. First, the object type and potential of interest was identified, e.g. the ellipsoidal Gaussian blob discussed in Appendix C. Second, the Mathematica® computational software was used to construct the image. This required tabulating the image plane quantities ($x$, $y$, $I/I_0$), all of which are functions of the object plane coordinates ($x_0$, $y_0$), over a rectangular grid in ($x_0$, $y_0$) that was at least a few times larger than the object size $a$. The Mathematica function ListDensityPlot was used to plot the image intensity $I/I_0$ at the specified points ($x$, $y$). This produced grayscale images that were then log compressed to approximate the response of actual film to proton dose [Hey 2008] and auto-scaled for easier viewing.

For simple cases (e.g. Figures 3 and 11) one can calculate the image plane quantities by using the "ready-made" equations that we provide in this paper. For more complicated cases (e.g. Figure 4, which is a linear combination of Gaussian blobs) we started from an equation for the potential and then used Mathematica to symbolically integrate and then differentiate as required to obtain expressions for the deflection angles $\alpha$. Once the angles $\alpha$ were obtained, further differentiation was performed to construct the Jacobian and then we proceeded with the image generation as described above.

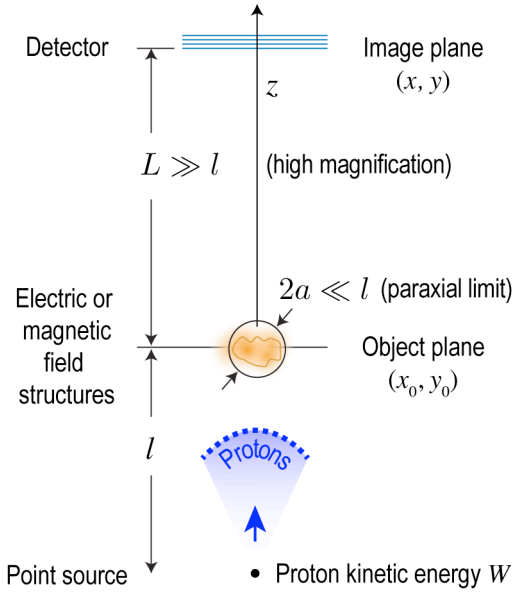


Fig. 1 (Color online) The geometry of a typical laser-plasma experiment where a point source of protons is used to image three-dimensional electric and magnetic field structures of size $2a$ in a plasma of interest. The proton source and the plasma are separated by a distance $l$.

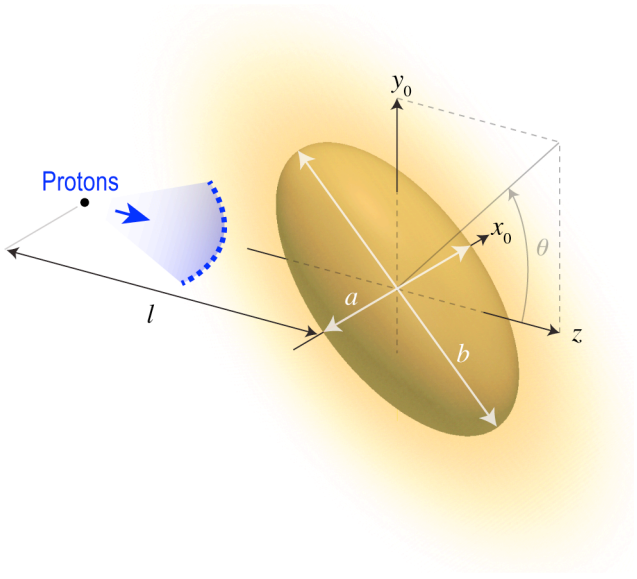


Fig. 2 (Color online) A three-dimensional ellipsoidal Gaussian blob with a contour at the $0.5\varphi_0$ equipotential surface. The aspect ratio $b/a = 2$, and the axis of the ellipsoid is tilted about the $x_0$-axis by an angle $\theta = 45°$ with respect to the $z$-axis.

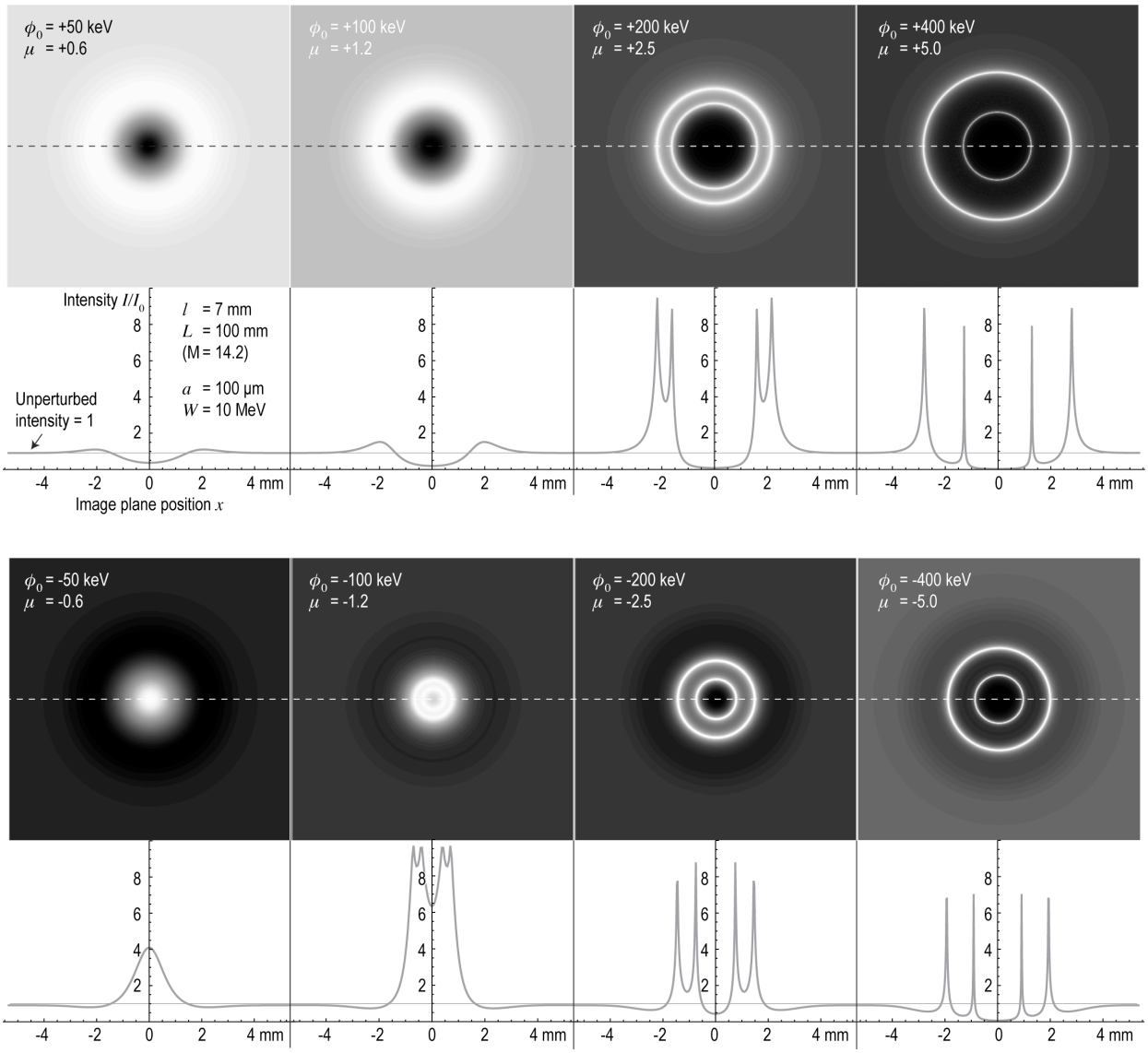


Fig. 3. Some characteristic images formed by spherically symmetric ($a$=$b$) Gaussian blobs of electric potential. Strong variations in intensity can be observed even without a caustic being formally generated. Shown here is a progression of proton images from the weak to the strong deflection regimes, for positive (upper panel) and negative (lower panel) electric fields. At low normalized potentials ($\mu < 1$) the behavior is linearly defocusing (focusing) for positive (negative) fields. Caustics form in the strongly nonlinear intermediate regime ($\mu > 1$). In the very strongly deflecting regime ($\mu \approx 10$, not shown) the caustics formed by positive and negative electric fields become indistinguishable, as is suggested by the increasing similarity of the images as a function of $\mu$ (e.g. compare the right-most panel). Parameters $l$, $L$, $a$, and $W$are common for all cases shown here.

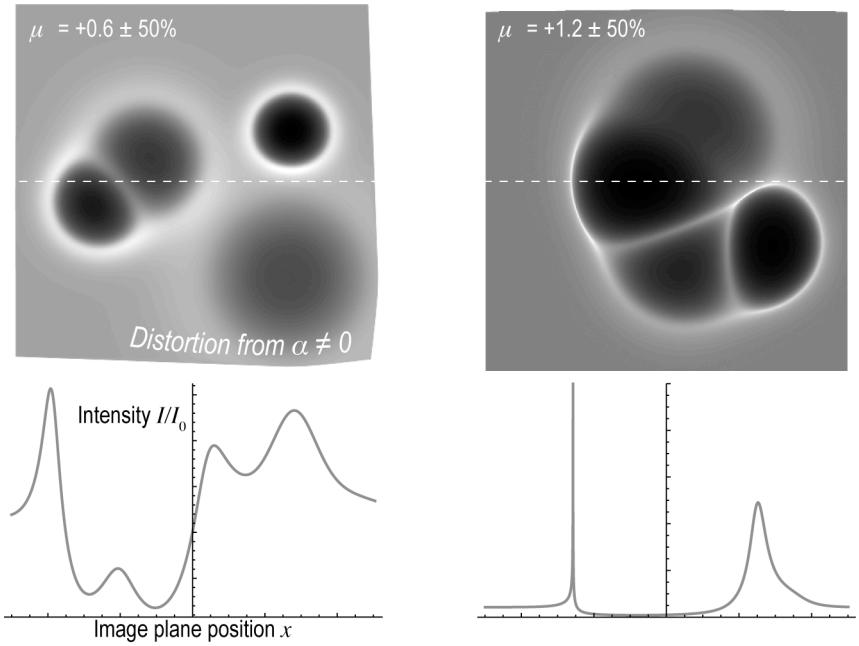


Fig. 4. Random constellations of four spherical Gaussian blobs of defocusing (positive) electric potential as seen in the image plane. To produce interesting images, the origins of the four blobs are scattered about with a Gaussian distribution over the interval $\{-2a, 2a\}$, and the size $a$ is randomized ± 50%, resulting in a corresponding variation in $\mu$. The non-linear nature of proton imaging and caustic formation can be seen in two features: the curved distortion at the image margins from $\alpha \neq 0$ (left panel) and the strange shapes produced by the overlap of multiple caustics (right panel). These shapes cannot be created by a linear superposition of deflections from spherically symmetric fields.

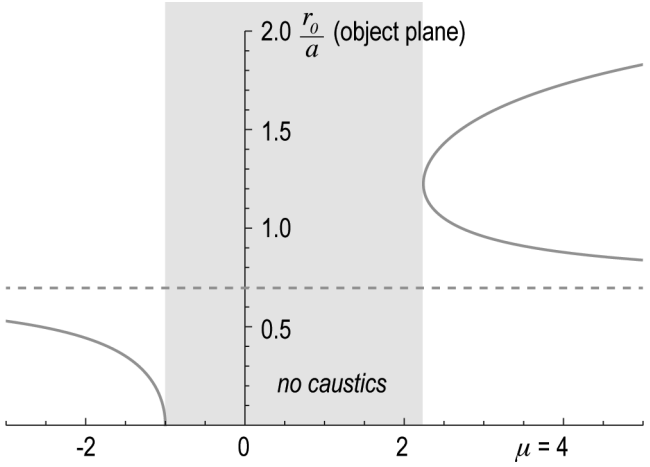

Fig. 5. The position in the object plane (normalized to the radius $a$) of a caustic from a spherical Gaussian blob, plotted parametrically in $r_0$ (Eq. 27) vs. the dimensionless potential $\mu$. For a focusing potential $\mu<0$, the caustic appears as a point, which then grows into a ring. For a defocusing potential, the caustic appears as a ring of a finite radius, which then splits in two rings. No caustic occurs in the object plane within the shaded region Grayscale images for these cases are shown in Fig. 3, projected to the image plane.

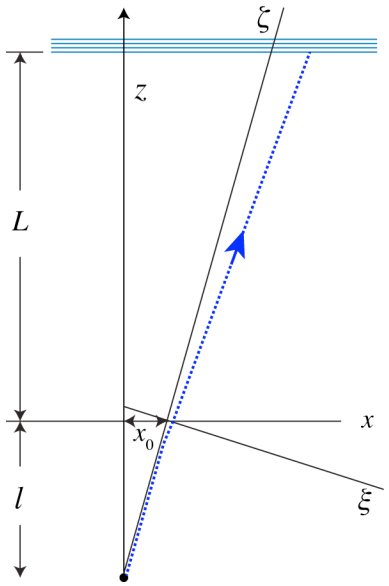


Fig. 6 (Color online). Illustration of the geometry of the higher-order corrections.

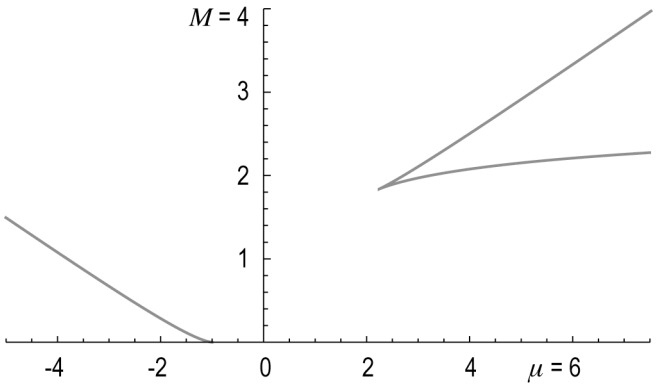

Fig. 7. Normalized magnification parameter $M$ vs the dimensionless potential $\mu$, plotted parametrically in $r_0$ (Eqns. A.1 and 27). A focusing potential corresponds to negative values of $\mu$.

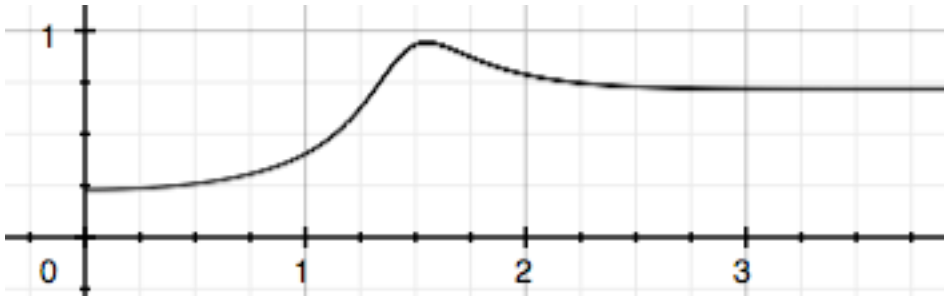


Fig. 8. The intensity distribution in the image plane at a potential amplitude insufficient for caustic formation.

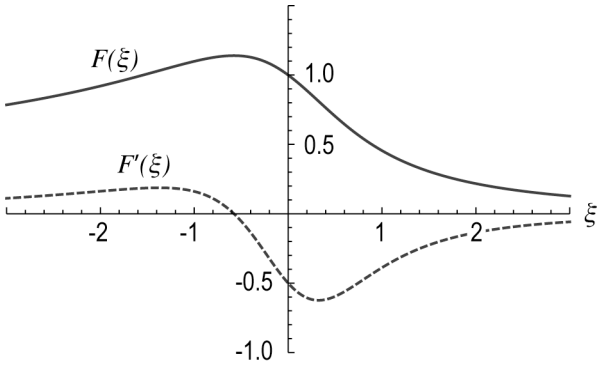


Fig. 9 The function $F$ (solid line) and its derivative $F'$ (dashed line) as a function of the distance $\xi$ to the boundary, normalized to the width parameter $h$.

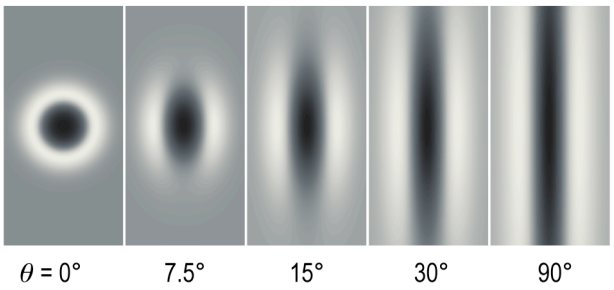

Fig. 10. Sequential rotation of a very ellipsoidal (aspect ratio $b/a$ = 10) Gaussian electric potential blob from the end-on view ($\theta$ = 0°) to the side-on view ($\theta$ = 90°) in the weak deflection regime ($\mu$ = +0.12) The side-on view approximates an infinite cylinder with a radially Gaussian profile, for the narrow field of view shown here.

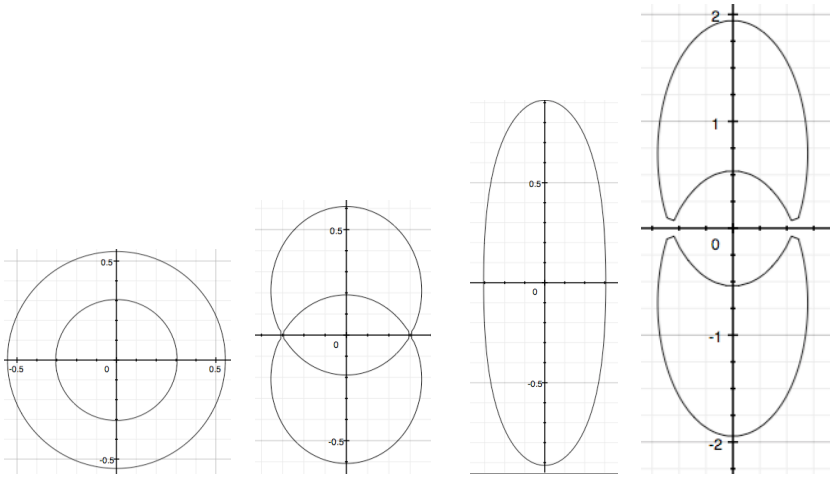


Fig 11. Several characteristic shapes of the caustics for the focusing potential (i.e., negative in case of ions). The left-most curve corresponds to a spherically-symmetric potential; the second curve corresponds to $a/d$=0,9; the third curve corresponds to $a/d$=0.6; the fourth curve corresponds to the same $a/d$, but larger absolute value of the potential.

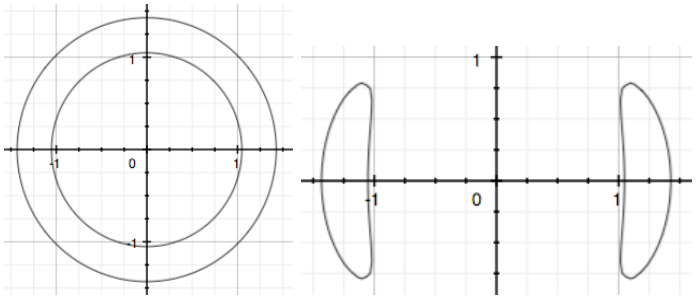


Fig. 12. The shape of caustics for the defocusing potential. The first picture corresponds to a spherically-symmetric blob, the second corresponds to a blob elongated along the $y$ axis. The absolute value of the potential is 1.8 times higher than in the first four panels in Fig. 11.

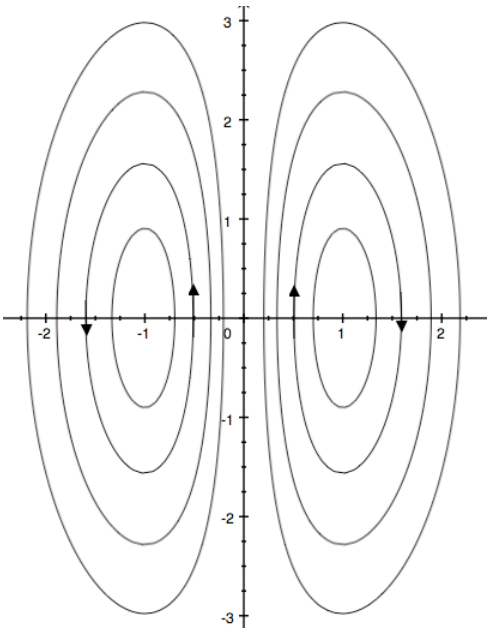


Fig. 13. Streamlines of the current density for a Gaussian magnetic blob. The magnetic field has only an azimuthal component, and the vector potential can be chosen so as to have only an axial component.

## References


M. Borghesi et al., "Laser-Driven Proton Beams: Acceleration Mechanism, Beam Optimization, and Radiographic Applications," *IEEE Transactions on Plasma Science*, vol. 36, no. 4, pp. 1833-1842, Aug. 2008.

M. Borghesi et al., "Multi-MeV Proton Source Investigations in Ultraintense Laser-Foil Interactions," *Physical Review Letters*, vol. 92, no. 5, p. 055003, Feb. 2004.

C. A. Cecchetti et al., "Magnetic field measurements in laser-produced plasmas via proton deflectometry," *Physics of Plasmas*, vol. 16, p. 043102, 2009.

C. Constantin et al., "Collisionless interaction of an energetic laser produced plasma with a large magnetoplasma," *Astrophysics and Space Science*, vol. 322, pp. 155-159, Mar. 2009.

C. D. Gregory et al., "Laser-driven plasma jets propagating in an ambient gas studied with optical and proton diagnostics," *Physics of Plasmas*, vol. 17, p. 052708, 2010.

D. S. Hey et al., "Use of GafChromic film to diagnose laser generated proton beams," *Review of Scientific Instruments*, vol. 79, p. 053501, 2008.

T. N. Kato and H. Takabe, "Nonrelativistic Collisionless Shocks in Unmagnetized Electron-Ion Plasmas," *The Astrophysical Journal*, vol. 681, no. 2, p. L93-L96, Jul. 2008.

Y. Kuramitsu et al., "Time Evolution of Collisionless Shock in Counterstreaming Laser-Produced Plasmas," *Physical Review Letters*, vol. 106, no. 17, p. 175002, Apr. 2011.

C. K. Li et al., "Proton radiography of dynamic electric and magnetic fields in laser-produced high-energy-density plasmas," *Physics of Plasmas*, vol. 16, p. 056304, 2009.

C. K. Li et al., "Diagnosing indirect-drive inertial-confinement-fusion implosions with charged particles," *Plasma Physics and Controlled Fusion*, vol. 52, p. 124027, Dec. 2010.

L. D. Landau and E. M. Lifshitz, *The Classical Theory of Fields, Fourth Edition: Volume 2*, 4th ed. Butterworth-Heinemann, 1980.

B. Loupias et al., "Experimental results to study astrophysical plasma jets using Intense Lasers," *Astrophysics and Space Science*, vol. 322, pp. 25-29, Mar. 2009.
J. S. Ross POP 2012 (invited talk POP)

A. J. Mackinnon et al., "Proton radiography as an electromagnetic field and density perturbation diagnostic (invited)," *Review of Scientific Instruments*, vol. 75, p. 3531, 2004.

J. . Nye, *Natural Focusing and Fine Structure of Light: Caustics and Wave Dislocations*, 1st ed. Taylor & Francis, 1999.

M. V. Medvedev and A. Loeb, "Generation of Magnetic Fields in the Relativistic Shock of Gamma-Ray Burst Sources," *The Astrophysical Journal*, vol. 526, no. 2, pp. 697-706, Dec. 1999.

S. S. Moiseev and R. Z. Sagdeev, "Collisionless shock waves in a plasma in a weak magnetic field," *Journal of Nuclear Energy. Part C, Plasma Physics, Accelerators, Thermonuclear Research*, vol. 5, no. 1, pp. 43-47, Jan. 1963.

H.-S. Park et al., "Studying astrophysical collisionless shocks with counterstreaming plasmas from high power lasers," *High Energy Density Physics*, vol. 8, no. 1, pp. 38-45, Mar. 2012.

L. Romagnani et al., "Proton Probing Measurement of Electric and Magnetic Fields Generated by ns and ps Laser-Matter Interactions," *Laser and Particle Beams*, vol. 26, no. 2, pp. 241-248, 2008.

M. Roth, "The diagnostics of ultra-short pulse laser-produced plasma," *Journal of Instrumentation*, vol. 6, p. R09001-R09001, Sep. 2011.

D. D. Ryutov, N. L. Kugland, H.-S. Park, S. M. Pollaine, B. A. Remington, and J. S. Ross, "Collisional current drive in two interpenetrating plasma jets," *Physics of Plasmas*, vol. 18, p. 104504, 2011.

Prepared by LLNL under Contract DE-AC52-07NA27344.